Tissue Elasticity Reconstruction Based on Ultrasonic Displacement and Strain Images

A. R. Skovoroda, S. Y. Emelianov, and M. O'Donnell, *Fellow, IEEE*

Abstract— A method is presented to reconstruct the elastic modulus of soft tissue based on ultrasonic displacement and strain images. Incompressible and compressible media are considered separately. Problems arising with this method, as well as applications to real measurements on gel-based, tissue equivalent phantoms, are given. Results show that artifacts present in strain images can be greatly reduced using a hybrid reconstruction procedure based on numerical solution of the partial differential equations describing mechanical equilibrium of a deformed medium.

I. INTRODUCTION

IMAGING internal soft tissue displacements and strains resulting from mechanical forces applied to the body surface is rapidly developing into a new diagnostic modality [1]–[32]. Internal deformational images, however, emphasize **both** the spatial distribution of the Young's or shear modulus **and** global boundary conditions, including mechanical constraint of the body, its geometry, the types of external and internal forces, etc. That is, displacement and/or strain images may exhibit significant artifacts due to global boundary conditions, as discussed in [28], [29]. The primary objective of the work described here is to significantly reduce artifacts in elasticity images by directly reconstructing and imaging the elastic Young's modulus. Although absolute quantitation may ultimately be important for certain applications, differential diagnosis based on tissue elasticity will probably be based on relative modulus reconstruction. We strongly believe that artifacts due solely to global boundary conditions must be minimized for elasticity imaging to become a routine diagnostic procedure.

Computing the mechanical properties of a medium based on its response to mechanical action can be posed in a number of ways. In this paper we have used two different formulations of elasticity reconstruction. The first starts with the complete spatial distribution of the strain tensor or displacement; the second uses limited experimental data such as an image of a single strain component. Because of physical limitations inherent in measuring internal displacements and

strains with an ultrasound imaging system, i.e. limitations of traditional longitudinal speckle tracking algorithms for large absolute displacements and the poor accuracy of lateral displacement measurements (due to lower spatial frequencies laterally), work to date has focused on estimating elastic moduli with limited deformational information [17], [21], [24], [28], [29]. Based on simplified models of both the elastic modulus distribution in the body and the mechanical boundary conditions, these methods are accurate only in limited applications or, otherwise, produce large artifacts in the elasticity reconstruction [29]. Consequently, expanded reconstruction methods are needed to handle more complex objects and boundary conditions. In this paper, we explore new reconstruction methods based on quantitative strain and displacement images.

In the theory section, the general approach to reconstruction based on the common model of linear, elastic, isotropic, incompressible media is presented. Compressible media are considered in Appendix I. Following that, a hybrid reconstruction procedure independent of global boundary conditions is described. Also presented here are practical methods to estimate the elastic modulus using only limited experimental data, i.e., only accurate measurements of the axial displacement and longitudinal strain. Some additional cases of elasticity reconstruction based on limited measurements are considered in Appendix II. The details of the hybrid reconstruction method based on internal tissue displacement and strains estimated from ultrasonic images is described in the next section. In the results section, a specific reconstruction algorithm appropriate for a plane strain state is tested using experimental images of internal deformations in tissue equivalent, gel-based phantoms. These displacement and strain images were made with an ultrasound-based deformational imaging system described in [27]–[29]. The paper concludes with a discussion of the results.

II. THEORY

Consider a three-dimensional (3-D) volume V of deformed media with the displacement vector $\mathbf{U} = (u_1, u_2, u_3)$ in Cartesian coordinates $\mathbf{X} = (x_1, x_2, x_3)$. Volume V can be either the entire mechanical body, or a region of interest (ROI) inside the object under study.

The most general form of Newton's 2nd law describing the motion of a mechanical body under static deformation (i.e., the equilibrium condition) is,

$$\sum_{j=1}^{3} \sigma_{ij,j} + f_i = 0, \quad i = 1, 2, 3 \tag{1}$$

where σ_{ij} is one component of the 2nd ranked stress tensor and f_i is the body force per unit volume acting on the body in the x_i direction [29], [33]–[35]. This model applies for soft tissue at a spatial scale sampled by diagnostic ultrasound (i.e., at a scale greater than or comparable to an ultrasound wavelength). In (1), and the entire paper, the lower index after a comma means differentiation with respect to the corresponding spatial coordinate. Equation (1) must be satisfied at every internal point of the body. We should also note here that most soft tissues and tissue-like materials (with the exception of lung, for example) can be considered incompressible [36], i.e., the Poisson's ration is equal to 0.5. In the main body of the paper only incompressible media are considered. Compressible media (i.e., Poisson's ratio less than 0.5) are discussed separately in Appendix I. Treating slightly compressible media as completely incompressible greatly simplifies the partial differential equations describing internal deformations and permits stable numerical solution of these equations. A complete compressible description, although theoretically more accurate, often leads to unstable numerical solution in the limit that the Poisson's ratio approaches 0.5.

Assuming linear elasticity, the components of the stress tensor in an isotropic, continuous, incompressible medium under static deformation are:

$$\sigma_{ij} = p\delta_{ij} + 2\mu\varepsilon_{ij}, \tag{2}$$

where p is the static internal pressure, defined as [37]

$$\lim_{\substack{\lambda/\mu\to\infty \\ div\mathbf{U}\to 0}} [\lambda(div\mathbf{U})] = p. \tag{3}$$

In (2) δ_{ij} is the Kronecker delta symbol and ε_{ij} is one component of the 2nd ranked symmetric strain tensor, defined as

$$\varepsilon_{ij} = \frac{1}{2}\left(\frac{\partial u_i + \partial u_j}{\partial x_j + \partial x_i}\right) \tag{4}$$

where u_i is one component of displacement vector $\mathbf{U} = (u_1, u_2, u_3)$. Note that a pressure term must be included in (2) to fully describe deformations in incompressible media. Also, some tissues, such as muscle, are anisotropic [35], necessitating a more general stress-strain relationship [33], [34]. In this paper, however, only isotropic media are considered.

In (2) and (3) the parameters λ and μ are Lame coefficients. In general, the longitudinal Lame coefficient λ and shear modulus μ describe the elastic behavior of a mechanical body. However, with assumption (3), any statically deformed, isotropic, continuous, incompressible mechanical body can be completely characterized by a spatial distribution of a **single** material parameter, either shear modulus μ or Young's modulus E since they are simply proportional to each other, i.e. $E = 3\mu$. Note that this is a fundamental difference between incompressible and compressible media. That is, the Young's modulus completely describes the static elastic properties of soft tissue, where its value may vary widely between different tissues (see, for example, reference [31]).

In addition, the incompressibility condition leads to the following relationship between displacement or strain components

$$div\mathbf{U} = \varepsilon_{11} + \varepsilon_{22} + \varepsilon_{33} = u_{1,1} + u_{2,2} + u_{3,3} = 0. \tag{5}$$

The main goal of elasticity imaging is to reconstruct the elastic modulus of any desired tissue region using available measurements of strain and displacement components. The Young's modulus E is an arbitrary function of position, i.e.

$$E(\mathbf{X}) = E_0 k(\mathbf{X}) \tag{6}$$

where E_0 is a constant and $k(\mathbf{X})$ is not generally a continuous function. Elasticity image reconstruction, therefore, centers on estimating $k(\mathbf{X})$.

Elasticity reconstruction in an isotropic medium must accurately represent both continuous and discontinuous changes in the modulus. Both types of spatial variation are illustrated in Fig. 1 for a single abnormality (i.e., inclusion) in an otherwise homogeneous medium. Small fluctuations in the modulus throughout the image plane represent local changes not indicative of true material differences. In Fig. 1(a), a clearly bounded inhomogeneity ("inclusion") with a discontinuous change in elastic modulus is illustrated. For this type of abnormality the magnitude of spatial changes in the elastic modulus at the boundary is much larger than any small scale fluctuations present. In contrast, a continuous inclusion with finite derivatives everywhere is presented in Fig. 1(b). Depending on the size and elasticity contrast of the inclusion, derivatives in the elastic modulus may be only slightly larger than small scale fluctuations in the medium. Both types of inclusion are important, however, and represent reasonable assumptions for a large set of tissue abnormalities. Due to elasticity variability and errors in strain measurement, reconstruction approaches for these two types of abnormalities may differ.

A. Bounded Inhomogeneities

We focus first on local, **clearly bounded** inclusions having a boundary $\mathbf{G}$ and residing in tissue with otherwise smoothly varying mechanical characteristics, as illustrated in Fig. 1(a). For this type of inclusion the unknown $k(\mathbf{X})$ is not a continuous function, i.e. it has a discontinuity at the boundary $\mathbf{G}$. Note that the position of the boundary $\mathbf{G}$ is also unknown *a priori* and needs to be determined. Therefore, the reconstruction problem reduces to detecting the unknown inclusion boundary and, consequently, reconstructing the unknown Young's modulus at this boundary.

The stress continuity condition at the boundary $\mathbf{G}$ has the form [34]:

$$\sum_{j=1}^{3} [\sigma_{ij}]n_j = \sum_{j=1}^{3} (\sigma_{ij}^{ext} - \sigma_{ij}^{int})n_j = 0, \ i = 1, 2, 3 \tag{7}$$

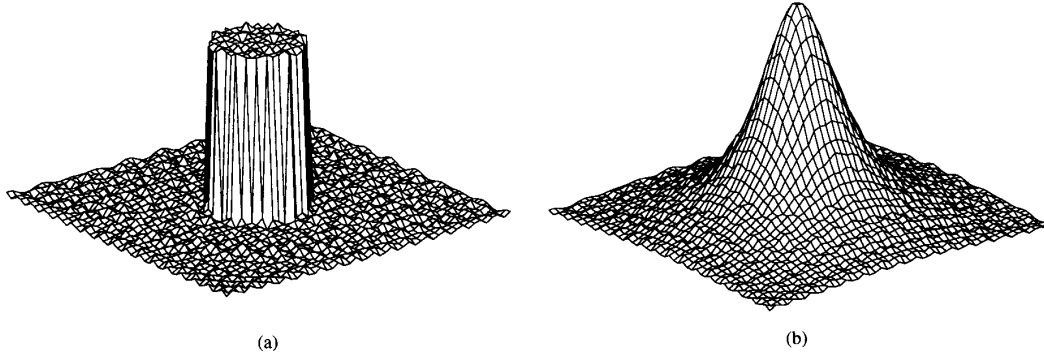where the square parentheses denote discontinuity of the corresponding external and internal terms at boundary points

Fig. 1. Elasticity distribution for (a) discontinuous, i.e., clearly bounded and (b) continuous inclusions.

$\mathbf{X_G} \subset \mathbf{G}$, and n_j is the jth component of the unit normal vector $\mathbf{n} = (n_1, n_2, n_3)$ at the boundary. In this and the following equations superscripts "int" and "ext" refer to internal and external variables at boundary points. Note that for any other point of the volume V inside or outside the inclusion, the stress continuity condition (7) is automatically satisfied for any arbitrarily chosen direction of a normal vector.

Assuming an incompressible, isotropic medium, substituting expression (2) into (7), and combining the results, the stress continuity condition becomes:

$$p^{ext}n_1 + 2\mu^{ext}(\varepsilon_{11}^{ext}n_1 + \varepsilon_{12}^{ext}n_2 + \varepsilon_{13}^{ext}n_3)$$
$$= p^{int}n_1 + 2\mu^{int}(\varepsilon_{11}^{int}n_1 + \varepsilon_{12}^{int}n_2 + \varepsilon_{13}^{int}n_3)$$
$$p^{ext}n_2 + 2\mu^{ext}(\varepsilon_{12}^{ext}n_1 + \varepsilon_{22}^{ext}n_2 + \varepsilon_{23}^{ext}n_3)$$
$$= p^{int}n_2 + 2\mu^{int}(\varepsilon_{12}^{int}n_1 + \varepsilon_{22}^{int}n_2 + \varepsilon_{23}^{int}n_3)$$
$$p^{ext}n_3 + 2\mu^{ext}(\varepsilon_{13}^{ext}n_1 + \varepsilon_{23}^{ext}n_2 + \varepsilon_{33}^{ext}n_3)$$
$$= p^{int}n_3 + 2\mu^{int}(\varepsilon_{13}^{int}n_1 + \varepsilon_{23}^{int}n_2 + \varepsilon_{33}^{int}n_3). \quad (8)$$

Since the pressure p cannot be directly measured by imaging systems, it is analytically eliminated from the stress discontinuity equations resulting in the following pair of equations [26]:

$$\Gamma[n_1n_2(\varepsilon_{11}^{ext} - \varepsilon_{22}^{ext}) + [(n_2)^2 - (n_1)^2]$$
$$\cdot \varepsilon_{12}^{ext} + n_3(n_2\varepsilon_{13}^{ext} - n_1\varepsilon_{23}^{ext})] = n_1n_2(\varepsilon_{11}^{int} - \varepsilon_{22}^{int})$$
$$+ [(n_2)^2 - (n_1)^2]\varepsilon_{12}^{int} + n_3(n_2\varepsilon_{13}^{int} - n_1\varepsilon_{23}^{ext})$$
$$\Gamma[n_1n_3(\varepsilon_{11}^{ext} - \varepsilon_{33}^{ext}) + [(n_3)^2 - (n_1)^2]$$
$$\cdot \varepsilon_{13}^{ext} + n_2(n_3\varepsilon_{12}^{ext} - n_1\varepsilon_{23}^{ext})] = n_1n_3(\varepsilon_{11}^{int} - \varepsilon_{33}^{int})$$
$$+ [(n_3)^2 - (n_1)^2]\varepsilon_{13}^{int} + n_2(n_3\varepsilon_{12}^{int} - n_1\varepsilon_{23}^{int}). \quad (9)$$

In (9) the ratio of shear or Young's moduli, $\mu^{ext}/\mu^{int} = E^{ext}/E^{int}$, is denoted by Γ. Compressible media are treated separately in Appendix I.

Both inclusion boundary detection and Young's modulus reconstruction at this boundary are based on (9) and performed in two steps. First, experimentally derived (9) are solved with respect to Γ for an arbitrarily chosen direction of the normal vector $\mathbf{n} = (n_1, n_2, n_3)$. At any boundary points where the direction of the "testing" normal vector coincides with the direction of the real normal vector, the true value of Γ is obtained. At other points, however, the value Γ will not represent the exact value but will highlight inclusion boundaries.

This procedure can be repeated for several directions of the normal vector to complete boundary detection. Next, after the inclusion boundary is identified, the true value of Γ can be calculated at boundary points since the direction of the normal vector will be predicted after the boundary detection procedure previously described. Note that if all components of the strain tensor are known, the first equation in (9) can be used to detect the boundary of the inclusion and then determine the value of Γ (i.e., relative Young's modulus ratio at this boundary), and the second one to estimate the accuracy of experimental strain measurements in the neighborhood of the boundary point $\mathbf{X_G}$. Also, if the mechanical properties do not vary significantly inside the inclusion, reconstruction is complete since the Young's modulus at the boundary is found.

Equation (9) can also be used for boundary detection of more complicated elasticity inhomogeneities. If the Young's modulus changes smoothly both inside and outside the inclusion, then experimentally derived (9) solved with respect to Γ for any chosen direction of the vector $\mathbf{n}$ will give smoothly varying results everywhere except at boundary intersection points. Although the value Γ will not represent the exact value, this will highlight inclusion boundaries. In general, this approach produces a qualitative reconstruction, i.e., boundary detection, and will require Young's modulus reconstruction at every point of the volume V or any chosen region of interest. This is considered in the following section. Nevertheless, such information derived from measured strain images can be extremely important in those cases where the inclusion or other tissue structures cannot be directly visualized by the imaging system [28], [29].

In (8), (9) a linear stress-strain relation is assumed, but no assumption is made about the strain-displacement relation. Also, only the strain distribution in the immediate neighborhood of the boundary is needed to reconstruct the Young's modulus at this boundary. Consequently, this method can be used without requiring small strain magnitude as long as the stress-strain relation is still approximately linear, i.e., described by (2). In most soft elastic materials such as tissue, the strain reaches a limiting value ε_d, where the strain-displacement relation (4) is no longer valid, before the stress-strain relation goes nonlinear. Only upon reaching a second, higher limiting strain value, ε_s, do both simple strain-displacement (4) and

linear stress-strain (2) relations breakdown [33], [35], [38], [39]. Therefore, methods based on stress continuity (8), (9) are valid up to relatively high strain magnitude (for example, up to 20% [38]). Note that limiting strain values vary for different tissues. The use of high strains is extremely important in clinical applications where large displacements can enhance the signal to noise ratio of quantitative strain images [28].

Equation (9) shows that for an arbitrary deformed state, reconstructing boundary values of the Young's modulus for clearly bounded inhomogeneities requires measurement of all strain components in the neighborhood of the boundary $\mathbf{G}$. For a general, three-dimensional inclusion, this means complete three-dimensional strain data. To reconstruct the Young's modulus in a single plane, all displacement components must only be measured in three close parallel planes intersecting the volume V. From measurements in these three planes, coefficients needed for reconstruction in the central plane based on (9) can be calculated numerically with second order accuracy. General three-dimensional reconstruction of the inclusion boundary can be done by moving the imaging planes in parallel. Note that only a pair of close parallel planes can also be used for numerical reconstruction in a single plane, but will, however, exhibit greater error since less accurate finite differences will be used to approximate all derivatives.

B. Distributed Inhomogeneities

Not all inhomogeneities will exhibit a clear boundary and, therefore, reconstruction of an isotropic medium with **spatially continuous** changes in the Young's modulus is required. An example of such a distribution is given in Fig. 1(b). For this type of reconstruction the function $k(\mathbf{X})$ in (6) is assumed to be continuous with well defined spatial derivatives.

Using the equations defining a linear, incompressible elastic medium, the equilibrium condition (1) can be rewritten in the form [26]:

$$2\varepsilon_{12}(k_{,11} - k_{,22}) + 2(u_{2,2} - u_{1,1})k_{,12}$$
$$+ 2\varepsilon_{23}k_{,13} - 2\varepsilon_{13}k_{,23} + (\Delta u_2 + \omega_{12,1})k_{,1}$$
$$- (\Delta u_1 - \omega_{12,2})k_{,2} + \omega_{12,3}k_{,3} + \Delta\omega_{12}k + F_{12} = 0$$
$$2\varepsilon_{13}(k_{,11} - k_{,33}) + 2\varepsilon_{23}k_{,12}$$
$$+ 2(u_{3,3} - u_{1,1})k_{,13} - 2\varepsilon_{12}k_{,23}$$
$$+ (\Delta u_3 + \omega_{13,1})k_{,1} + \omega_{13,2}k_{,2}$$
$$- (\Delta u_1 - \omega_{13,3})k_{,3} + \Delta\omega_{13}k + F_{13} = 0$$
$$2\varepsilon_{23}(k_{,22} - k_{,33}) + 2\varepsilon_{13}k_{,12} - 2\varepsilon_{12}k_{,13}$$
$$+ 2(u_{3,3} - u_{2,2})k_{,23} + \omega_{23,1}k_{,1} + (\Delta u_3 + \omega_{23,2})k_{,2}$$
$$- (\Delta u_2 - \omega_{23,3})k_{,3} + \Delta\omega_{23}k + F_{23} = 0 \qquad (10)$$

where the pressure p is eliminated from this system of equations, and the following notations are used:

$$\omega_{12} = u_{2,1} - u_{1,2}, \omega_{13} = u_{3,1} - u_{1,3}, \omega_{23} = u_{3,2} - u_{2,3},$$
$$\Delta = \partial^2/(\partial x_1^2) + \partial^2/(\partial x_2^2) + \partial^2/(\partial x_3^2),$$
$$F_{12} = (3/E_0)(f_{2,1} - f_{1,2}), F_{13} = (3/E_0)(f_{3,1} - f_{1,3}),$$
$$F_{23} = (3/E_0)(f_{3,2} - f_{2,3}).$$

Analytical solution of (10) is not generally possible for an arbitrary spatial distribution of the elastic modulus $k(\mathbf{X})$. Note

also that this set of equations represents a boundary value problem and has an infinite number of solutions unless some boundary conditions for $k(\mathbf{X})$ are specified.

Complete numerical solution of these equations is possible if all components of the displacement vector and strain tensor are measured. It also requires that the boundary conditions for $k(\mathbf{X})$ be specified in the volume V. However, as considered in Appendix II, for some cases of Young's modulus distribution, numerical solution of (10) can be obtained in a single plane by discretizing all functions and computing spatial derivatives with finite differences to yield a set of simultaneous linear equations. That is, the complete displacement vector $\mathbf{U}$ must be accurately measured in at least three close parallel planes intersecting the volume V. Given complete displacement data in these planes and boundary conditions for $k(\mathbf{X})$ only in the central plane, all coefficients of the differential equations can be calculated numerically with second order accuracy and the elasticity distribution can be reconstructed in the central plane.

C. Hybrid Reconstruction

In practice, neither clearly bounded inclusions nor smoothly distributed inhomogeneities are complete models of elastic modulus variations. To handle more general cases, a hybrid procedure is used.

First, strain images are processed based on (9) to highlight boundaries between regions of different elastic modulus. If clearly bounded inclusions are present, then the Young's modulus can be obtained directly from (9) at points along the boundary. More importantly, this procedure can define regions of very small modulus variations (i.e., where Γ is close to one).

Following boundary detection, closed contours of small elasticity variations are defined. The total dimension of the contour must include several resolution cells of the final reconstruction. The modulus along these contours can be considered constant thereby providing a boundary condition for complete reconstruction of the elasticity within this region of interest (ROI) based on numerical solution of (10). The elasticity reconstructed in this way is the modulus **relative to** the modulus along the boundary. If the elastic modulus along this boundary is known (for example, if a specific tissue type such as fat constitutes the boundary region), then the reconstructed modulus is absolute. If the modulus along the boundary is not known, then the reconstruction remains relative. Even if the reconstruction is relative, potential artifacts in pure strain images due to the details of global boundary conditions (i.e., geometry of the object, types of external load, etc.) are removed.

Solution of (10) requires that both first and second order spatial derivatives of $k(\mathbf{X})$ be finite. If the ROI defined using (9) contains a bounded inclusion, then this may not be satisfied. To avoid this, a continuous elasticity distribution is forced by low pass filtering both displacement and strain data within the ROI prior to numerically solving (10). This filter effectively smoothes the reconstruction so that $k(\mathbf{X})$ is forced to be continuous with finite first and second order spatial derivatives. A negative consequence is that the reconstructed modulus is underestimated both along the boundary of large, clearly

bounded inclusions and within inclusions of spatial extent comparable to the dimensions of the filter. If necessary, the modulus can be estimated at these points from solution of (9), i.e., from the boundary detection process. This hybrid procedure allows local reconstruction of the elastic modulus within the body **without** knowledge of global boundary conditions.

D. Plane Strain State

If all components of the displacement vector and strain tensor are available, then the Young's modulus can be reconstructed with the hybrid procedure outlined above. However, current strain imaging systems based on ultrasonic speckle tracking are two-dimensional [17], [28], [29], and consequently, boundary detection and Young's modulus reconstruction within selected ROI's must be estimated based on displacement and strain data from a single imaging plane. To reconstruct the elastic modulus using current ultrasonic equipment either some symmetries must be assumed in the distribution of the Young's modulus, or the deformation pattern must be carefully controlled. Some simplifications to the general equations based on spatial symmetries in $k(\mathbf{X})$ permitting reasonable reconstruction from only two-dimensional displacement and strain measurements are considered in Appendix II. Below, we consider a specific type of deformation requiring displacement and strain data only in the $(x_1, x_2, 0)$ plane (i.e., $x_3 = 0$) to reconstruct the elastic modulus in that plane.

In some practically important cases the out of plane displacement u_3 is either zero or small compared to the others and the two in-plane components u_1 and u_2 do not vary significantly as a function of the out-of-plane coordinate. This is possible, for example, if one dimension of the region far exceeds the others and the character of the inhomogeneity as well as the manner of loading does not change or changes only slightly along this direction. An example of such a deformation is given in Fig. 2. Here a uniform surface displacement is applied along the long x_3 axis of a cylindrical medium. Fig. 2(a) shows a three-dimensional view of this deformation geometry and Fig. 2(b) and (c) illustrate two orthogonal cross sections. Two different cases are presented: a cylindrical inhomogeneity extending the entire length of the object and a spherical inhomogeneity placed at the center. For the cylindrical inhomogeneity, this deformation will accurately approximate a plane strain state for imaging at the central plane $x_3 = 0$ [28], [29]. For the spherical inclusion, it produces a weak approximation to a plane strain state. As will be demonstrated below, if a uniform surface displacement is applied then a plane strain state is a good approximation even if the inhomogeneity is not extremely long.

For a plane strain state, in-plane components u_1 and u_2 of the displacement vector $\mathbf{U}$ are functions only of x_1 and x_2, and $u_3 = 0$. Also, at the inclusion boundary only two components of the normal vector are nonzero, i.e., $\mathbf{n} = (n_1, n_2, 0)$. For these conditions, the second equation of (9) is automatically satisfied and the first one leads to the following.

$$\Gamma = \frac{n_1 n_2 (\varepsilon_{11}^{int} - \varepsilon_{22}^{int}) + [(n_2)^2 - (n_1)^2]\varepsilon_{12}^{int}}{n_1 n_2 (\varepsilon_{11}^{ext} - \varepsilon_{22}^{ext}) + [(n_2)^2 - (n_1)^2]\varepsilon_{12}^{ext}}. \quad (11)$$

In this case, (11) should be satisfied along the entire boundary of a clearly bounded inclusion contained in the plane.

Some additional simplifications based on the condition of incompressibility (5) are possible. For a plane strain state, the condition of incompressibility reduces to $\varepsilon_{11} + \varepsilon_{22} = 0$, and consequently, at any point along the boundary where two components of the normal vector are equal in magnitude, i.e., $(n_1)^2 = (n_2)^2$, (11) reduces to

$$\Gamma = \frac{E^{ext}}{E^{int}} = \frac{\varepsilon_{22}^{int}}{\varepsilon_{22}^{ext}}. \quad (12)$$

The parameter Γ is defined above as the ratio of Young's moduli of internal and external media at the boundary of the inclusion. That is, at any point where two components of the unit normal to the border of a clearly bounded inclusion are equal in magnitude, the Young's modulus can be accurately computed from a **single** component of the strain tensor. This is a key result since only a single component is accurately measured with current strain imaging systems [17], [28].

Accurate reconstruction of the Young's modulus based on (12) is only possible at special points. However, (12) can be generally used to detect inclusions since there will be large changes in Γ near the boundary over a wide range of n_1 and n_2. Following boundary detection, all points satisfying $(n_1)^2 = (n_2)^2$ can be identified. At these points the Young's modulus obtained from (12) represents an accurate estimate at the boundary. For all other points, the shear strain component ε_{12} should be taken into account. Nevertheless, the simple expression presented in (12) can be used to detect inclusion boundaries even if the inclusion exhibits significant but smooth spatial changes in the Young's modulus.

Following boundary detection and definition of a closed curve of constant elastic modulus, (10) must be solved numerically within all ROI's. For a plane strain state, where the displacement vector components are $u_1 = u_1(x_1, x_2)$, $u_2 = u_2(x_1, x_2)$, $u_3 = 0$, the set of (10) reduces to a single nontrivial equation:

$$(k_{,11} - k_{,22})(u_{1,2} + u_{2,1}) + 2k_{,12}(u_{2,2} - u_{1,1})$$
$$+ 2k_{,1}(u_{2,11} + u_{2,22}) - 2k_{,2}(u_{1,11} + u_{1,22})$$
$$+ k(u_{2,111} + u_{2,221} - u_{1,112} - u_{1,222})$$
$$+ F_{12} = 0$$
$$F_{13} = 0$$
$$F_{23} = 0. \quad (13)$$

Note that only two-dimensional in-plane displacement and strain measurements are needed to reconstruct the modulus in the plane $x_3 = 0$.

In actual ultrasonic strain imaging systems, one component of the displacement is measured with much higher accuracy than the other. This can create reconstruction error based on (13). Fortunately, this problem can be largely overcome because the incompressibility condition for a plane strain state is simply $u_{1,1} + u_{2,2} = 0$, where $u_{2,2}$ is the longitudinal strain component accurately measured within the image plane. Based on this, accurate measurements of the lateral u_1 component of
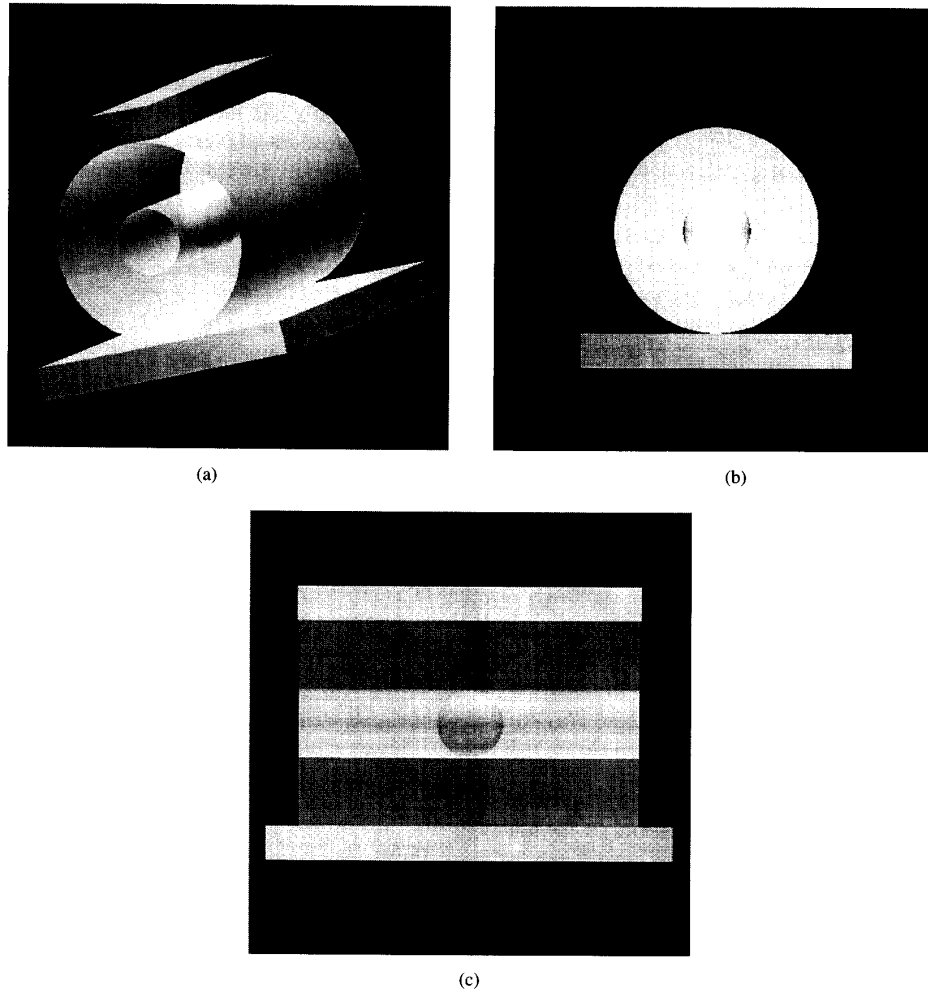
(a)

(b)

(c)

Fig. 2.   Schematic of a uniform deformation applied along the long x_3 axis of a cylinder. (a) Three-dimensional view of this deformation geometry. Two different cases are presented: a cylindrical inhomogeneity extending the entire length of the object, and a spherical inhomogeneity placed at the center, where a plane strain state is well approximated at the central cross-section of the object. (b) and (c) Illustrate two orthogonal cross-sections through the same object.

the displacement vector are needed along only one longitudinal curve to compute the in-plane distribution of the lateral displacement from the incompressibility equation.

The specific approach used to solve the 2nd order partial differential in (13) depends on the relative magnitudes of the coefficients in [40]. It is generally hyperbolic, although a degenerate (i.e., parabolic) case is possible. For an incompressible material, the degenerate case for the plane strain state corresponds to an in-plane translation with rotation of the volume as a rigid body. This means that the distribution of relative Young's modulus $k(\mathbf{X})$ cannot be reconstructed without knowledge of the internal pressure distribution for this special case, and, therefore, either the pressure must be measured and included into reconstruction, or different strain and displacement patterns must be created within the object using different boundary conditions. Note that there are some very specific cases where (13) will always be degenerate regardless of boundary conditions and, therefore, will require

measurements of the internal pressure distribution. Generally, however, the boundary defined from (12) produces a nondegenerate boundary value problem with a unique solution. Note also that (13) for the nondegenerate case represent a boundary value problem and, therefore, boundary conditions for $k(\mathbf{X})$ must be specified to determine the unique solution.

III. METHODS

Experiments were performed on a number of gel-based cylindrical phantoms; a detailed description of phantom fabrication is given in references [28], [29]. The results reported here were obtained from a specific set of phantoms illustrated in Fig. 3.

A. Homogeneous Phantom

A homogeneous cylinder 88 mm in diameter and 140 mm long was constructed from a 5.5% by weight gelatin concentration. A small amount of polystyrene microspheres
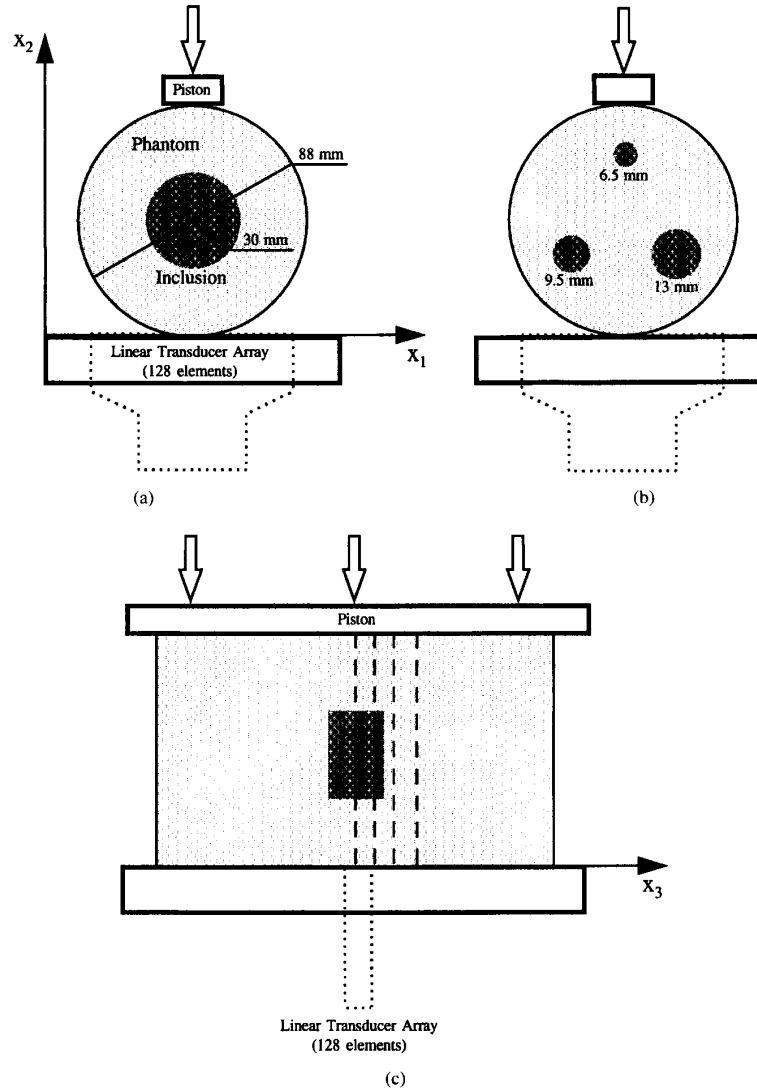
Fig. 3. Illustration of phantoms and deformation used in experiments. (a) Cross sectional view of the phantom with a single hard or soft inclusion. (b) Cross sectional view of the phantom with three hard inclusions of different size. In both cases the inclusions extend the entire length of the phantom. (c) Longitudinal view of the phantom with a short, 10 mm long cylindrical hard inclusion at the center. Four different imaging planes through the phantoms are also shown.

was added to act as ultrasonic scattering centers. This scatterer concentration remained the same for all phantom materials.

B. Phantom with a Single Hard Inclusion

First, a homogeneous phantom was constructed from a 5.5% by weight gelatin concentration. Then, a circular, longitudinal hole 30 mm in diameter was made in the center of the phantom. This hole was backfilled with 12% gelatin concentration producing a hard cylindrical inclusion extending the entire length of the phantom. The Young's modulus of the inclusion was estimated to be about three times larger than that of surrounding material. This estimate was based on an approximately linear dependence of the Young's modulus on gel concentration in this range [36].

C. Phantom with a Single Soft Inclusion

This phantom was constructed similar to previous phantoms with the only difference that 12% gelatin concentration was used for the surrounding material and 5.5% gelatin for a soft inclusion. Again, the 30 mm in diameter soft inclusion extended the entire length of the phantom, and the Young's modulus of the inclusion was estimated to be about 2.5–3.0 times smaller than that of surrounding material. The cross-sectional view of the phantom with a single either soft or hard inclusion is shown in Fig. 3(a), where dimensions are also given.

D. Phantom with Three Hard Inclusions

Three longitudinal holes of different diameter (6.5 mm, 9.5 mm and 13 mm) were made in an otherwise homo-

geneous cylindrical gel constructed from 5.5% by weight gelatin concentration. All three holes were backfilled with 12% gelatin producing hard inclusions of different size, as shown in Fig. 3(b). Once again, these inclusions extended the full length of the phantom.

E. Phantom with a Single Short, Hard Inclusion

A homogeneous cylinder with the same overall dimensions as the homogeneous phantom was constructed from 5.5% by weight gelatin concentration. Then, a circular, longitudinal hole 30 mm in diameter was made in the center of the phantom. The hole was backfilled with the same 5.5% gelatin concentration except for a small central part, backfilled with 12% by weight gelatin concentration, producing a hard, 10 mm long, cylindrical inclusion in the center of an otherwise homogeneous phantom. The central cross-section of the phantom with a single short inclusion closely corresponds to that shown in Fig. 3(a). A longitudinal view is presented in Fig. 3(c).

Each phantom was placed in a water tank with cylindrical axis perpendicular to the axis of a 3.5 MHz, 128 channel, 1-D transducer array attached to the bottom of the tank. The phantom was centered so that the image plane approximated the central plane perpendicular to the longitudinal axis of the cylindrical phantom. The tank was filled with water to provide contact between the array and phantom. Simple surface displacements were produced by a hydraulically driven piston contacting the phantom at the top center over the entire length of the cylinder, where movement of this piston was controlled by measuring ultrasonic pulse arrival time differences to the central array elements. This piston was a 14 mm wide, rigid, rectangular block extending the entire length of the phantom. The bottom of the phantom contacted the tank such that it did not move during piston displacement. The deformation at the central vertical plane of the phantom produced by this experimental system closely corresponds to the deformation geometry shown in Fig. 2 and approximates a plane strain state.

As discussed previously, traditional speckle tracking breaks down for large (compared to an acoustic wavelength) displacements because of both out-of plane motion and decorrelation effects due to finite strain [28]. To overcome these limitations, a large set of images were recorded with small relative displacements but significant total displacement from the beginning to end of the set. The results presented below used a large set of images spanning the total vertical piston displacement with 200–300 μm steps to quantitatively estimate the vertical displacement and the vertical longitudinal strain. These images were computed by properly accumulating differential displacement and strain estimates between two neighboring images of this large set spanning the total deformational range [28].

As reported previously [29], in the area of the central vertical plane of the phantom ($x_3 = 0$), the deformation pattern produced by the current system will closely approximate a plane strain state. For this state, components u_1 and u_2 of the displacement vector $\mathbf{U}$ are functions only of x_1 and x_2, and $u_3 = 0$. With these conditions, (12) may be used

for boundary detection of the inclusions, and (13) should completely describe deformations in the imaging plane.

After recording the set of ultrasound images and computing displacement and strain images from these data, the hybrid reconstruction of the Young's modulus proceeds in two subsequent steps. First, inclusion boundaries must be identified to define a nontrivial boundary value problem. That is, the closed curve of constant Young's modulus in the imaging plane must be defined. In all cases, the stress continuity condition was analyzed everywhere throughout the imaging plane using (12) to highlight inclusion boundaries. For every vertical line, i.e. x_1 is constant, and any position x_2 on this line, $\varepsilon_{22}(x_2 - h)$ and $\varepsilon_{22}(x_2 + h)$ were computed for a fixed step h. Using these definitions, the relative Young's modulus Γ was computed at every point according to (12), where Γ greater than 1.0 means that Young's modulus $E(x_2 + h)$ is greater than $E(x_2 - h)$ and Γ less than 1.0 means that Young's modulus $E(x_2 + h)$ is less than $E(x_2 - h)$.

Also, to minimize the effect of noise on these images, the value of Γ at each pixel is multiplied by the ratio of the average strain magnitude ($\bar{\varepsilon}_{22}$) in a large region about the pixel to the average strain along the center vertical line of the image. As discussed in [28], strain variance is relatively independent of strain magnitude. Based on a simple propagation of error analysis, the variance in Γ estimated by (12) is

$$\sigma_\Gamma^2 = (\Gamma^2 + 1)\left(\frac{\sigma_\varepsilon^2}{\bar{\varepsilon}_{22}^2}\right) \qquad (14)$$

where σ_ε^2 is the variance in the strain image. Clearly, in regions of small average strain $\bar{\varepsilon}_{22}$, normalizing by the average strain reduces large scale fluctuations in estimates of Γ. This normalization does not alter any results in high strain regions and only serves to minimize the effects of noise in low strain areas.

The second step is the actual reconstruction of the spatial distribution of the Young's modulus by solving (13) for unknown $k(\mathbf{X})$. To solve (13), both components of the displacement vector must be accurately measured throughout the entire image plane. However, only one component, in our experimental setup the vertical component $u_2(x_1, x_2)$, of the displacement vector is measured accurately using ultrasound speckle tracking [28]. Fortunately, the lateral displacement $u_1(x_1, x_2)$ can be estimated from the vertical displacement $u_2(x_1, x_2)$ using the incompressibility condition $u_{1,1} + u_{2,2} = 0$ and measurements of the lateral component of the displacement vector along any vertical longitudinal line. The specific program developed to solve (13) assumes that the lateral displacement $u_1(x_1, x_2)$ is zero along the central vertical axis of the image. This is a good approximation for all phantoms studied based on the vertical central plane symmetry of the experimental system. Only the phantom with three asymmetrically located hard inclusions [Fig. 3(b)] slightly violates this assumption. Nevertheless, for the top part of this phantom containing the smallest inclusion, this assumption will not be in a great error.

After defining the boundary of the region of interest (ROI) and the closed contour of uniform Young's modulus, (13) is discretized with a 2 mm grid spacing over the ROI, where
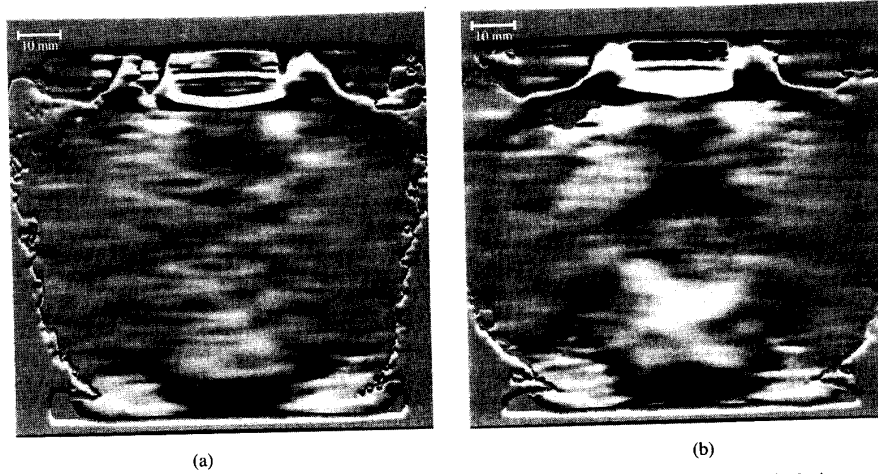
Fig. 4. Normalized elastic modulus (Γ) estimated in (a) homogeneous phantom and (b) phantom with a single hard inclusion.

all spatial derivatives are approximated by finite differences. Original displacement images are spatially low pass filtered to match this grid spacing before computing finite differences and to ensure that the model of a continuous elasticity modulus is well approximated. Also, it was assumed that F_{12} vanishes for our deformational system, where the phantom was immersed in water during the experiment and, therefore, gravitational and buoyancy forces cancel.

The linear set of equations resulting from the discretization of (13) is solved by iteration, where the error on each step is estimated by averaging the left-hand side of (13) over the entire grid using the current estimate of the Young's modulus distribution. From step to step, the entire modulus distribution over the full grid is updated based on changes in the average error.

IV. RESULTS

The hybrid reconstruction procedure was first tested on the homogeneous phantom and phantoms with a single long inclusion. In Fig. 4, Γ estimated using (12) for the homogeneous phantom [Fig. 4(a)] and the phantom with a single hard inclusion at the center [Fig. 4(b)] are presented. A step size h of approximately 0.4 mm was used for both images displayed over a 100 mm by 100 mm area, where the transducer array is at the bottom and the piston is located at the top. A quantitative gray scale is used for these images so that a Γ of 1.25 is pure white, a Γ of 0.75 is pure black and a Γ of 1.00 is mid-gray. Note that both images are displayed over the same dynamic range. There are large artifacts for both phantoms near the top and bottom of the image (i.e., near the piston and the constraining bottom plate). In these regions, high strain variations are formed by the boundary conditions resulting in erroneous estimates of Γ. Excluding these areas, there are striking differences between the Γ images of these two different phantoms. Near the top of the hard inclusion in Fig. 4(b) the value of Γ is significantly less than 1.0, indicating a transition from a soft to hard region. Correspondingly, near the bottom of the inclusion Γ is significantly larger than 1.0,

indicating a transition from hard to soft region. These are precisely the results expected for a single hard inclusion.

The boundaries of the single hard inclusion can be clearly seen in Fig. 4(b), but are even more visible if a different display format, such as that of Fig. 5, is used. In Fig. 5 the parameter Π, defined as

$$\Pi = \Gamma - 1 \qquad \text{for } \Gamma \geq 1$$
$$\Pi = 1/\Gamma - 1 \qquad \text{for } \Gamma < 1$$

is presented for the homogeneous phantom [Fig. 5(a) and (c)], phantom with single hard inclusion [Fig. 5(b)] and phantom with a single soft inclusion [Fig. 5(d)]. The first two [Fig. 5(a) and (b)] are the Π images for the images in Fig. 4 computed for a step size h of about 0.4 mm. These images are subjected to a threshold of 0.06 (i.e., $\Pi < 0.06$ is black and $\Pi \geq 0.06$ is white). Again, there are major differences between these two images and, clearly, the vertical boundaries of the inclusion in Fig. 5(b) are delineated. Differing from the previous two, the other two images of Fig. 5 [Fig. 5(c) and (d)] compare Π in the homogeneous phantom and the phantom with a single soft inclusion where a step size h of about 4 mm and threshold of 0.6 were used. Both top and bottom borders of the soft inclusion are highlighted in Fig. 5(d), but without the fidelity of Fig. 5(b). The homogeneous phantom in Fig. 5(c) does not exhibit any boundaries in the central area of the phantom for either 0.4 mm or 4 mm step sizes. The parameter Π, rather than Γ, is preferable for boundary detection since the same value is obtained at either hard to soft or soft to hard transitions. Note that each pair of images is displayed over exactly the same dynamic range.

Following boundary detection, reconstruction of the Young's modulus for the same phantoms is shown in Fig. 6. The reconstruction is based on numerical solution of (13), where it was assumed that the Young's modulus is uniform along the borders of the 40 by 40 mm square positioned at the center of the homogeneous phantom [Fig. 6(a)], phantom with the single hard inclusion [Fig. 6(b)] and phantom with
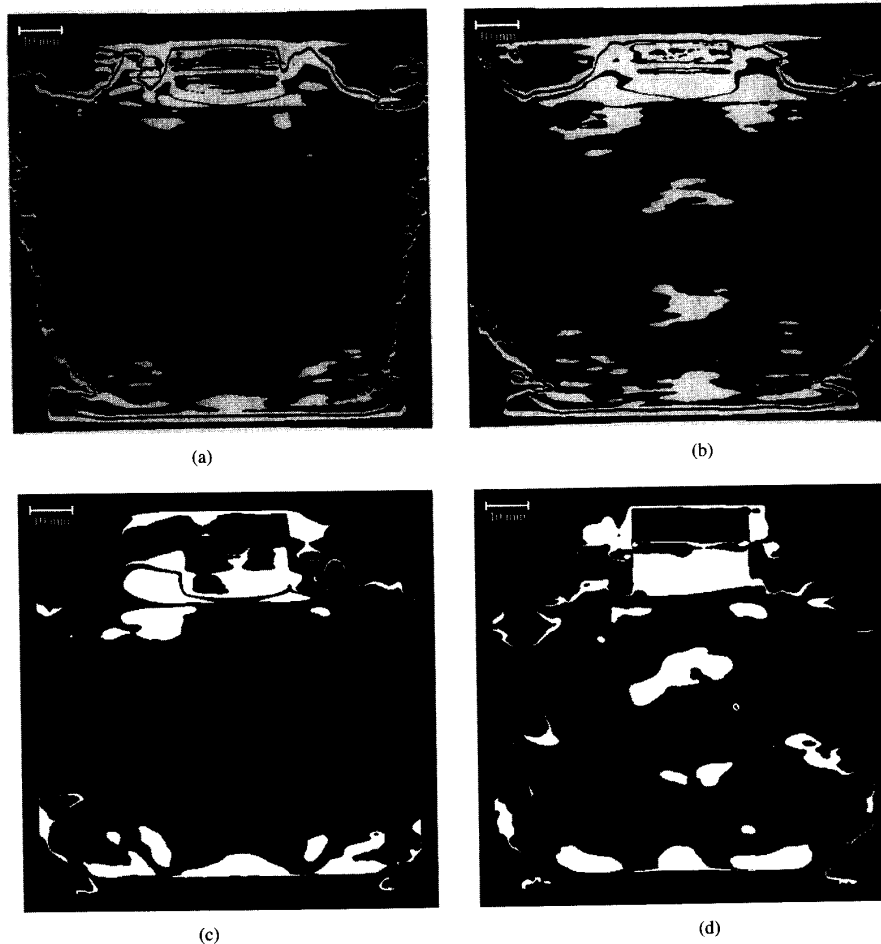
(a)

(b)

(c)

(d)

Fig. 5. Threshold differential elastic modulus (Π) estimates presented for two pairs of phantoms: (a) and (b) homogeneous phantom and phantom with a single hard inclusion, (c) and (d) homogeneous phantom and phantom with a single soft inclusion. Images in each pair are displayed over the same display dynamic range.

the single soft inclusion [Fig. 6(c)]. This square was chosen since it includes the boundaries detected in Figs. 4 and 5. The images in Fig. 6 represent the 40 by 40 mm region, where a logarithmic gray scale over the range $0.5 < E/E_0 < 2.1$ is used. The gray scale was selected so that the relative Young's modulus of 1.0 is mid-gray, dark areas represent softer material and bright areas harder material. The phantoms were subjected to 4–5 mm uniform vertical surface deformation applied along the entire length of the phantom. Both hard and soft inclusions are clearly visible. Moreover, changes in contrast for both inclusions are much greater than average error in the reconstruction of the homogeneous phantom. This is shown in Fig. 6(d), where reconstructed elasticity profiles along the central horizontal line are compared for the homogeneous phantom and phantoms with hard and soft inclusion. The results presented in Fig. 6 demonstrate that the reconstruction algorithm based on (13) reasonably matches the expected magnitude of relative Young's modulus in these phantoms.

As discussed previously [29], if a plane strain state is not present, i.e., an inappropriate model is used, then reconstruc-

tion based on (13) will be in error. To experimentally test the magnitude of these errors for a simple model system, the phantom with a short hard inclusion in the center of an otherwise homogeneous gel was used. This phantom was identical to the one with a single hard inclusion except that the inclusion was only about 10 mm long rather than the full length on the phantom. Four different planes of the phantom shown in Fig. 3(c) were imaged with a uniform 5 mm surface deformation, where the first imaging plane is at the center of the inclusion, the second plane is 3 mm displaced from the center of the inclusion but still within the inclusion (i.e., 2 mm from the edge of the inclusion), the other plane is 6 mm displaced from the center (i.e., 1 mm outside the inclusion) and, finally, the last imaging plane is 10 mm from the center of the inclusion (i.e., 5 mm outside the inclusion). The results of boundary detection and elasticity reconstruction in this phantom are presented in Fig. 7.

The first two [Fig. 7(a) and (b)] are boundary detection images, where the parameter Π was computed for a step size of 0.4 mm and displayed with a threshold of 0.06 (i.e., Π < 0.06
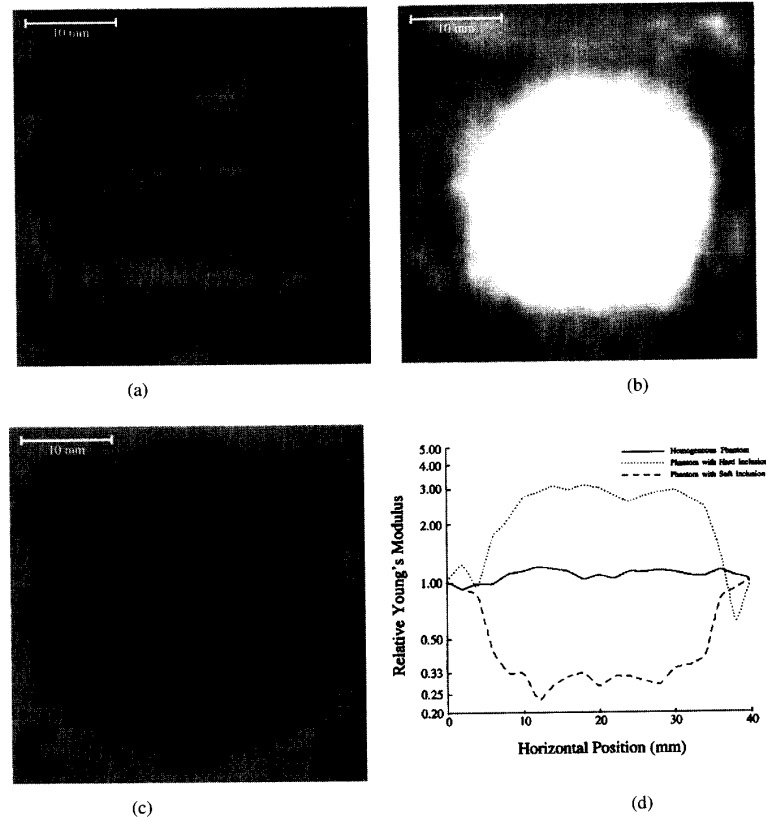
Fig. 6. Reconstructed images of the Young's modulus in the central plane of (a) homogeneous phantom, (b) phantom with a single hard inclusion, (c) phantom with a single soft inclusion. (d) Profiles of the reconstructed Young's modulus in the same phantoms along the central horizontal line are plotted on a semi-logarithmic scale. Phantoms were subjected to 4-5 mm uniform surface displacement.

is black and $\Pi \geq 0.06$ is white). Fig. 7(a) corresponds to the first imaging plane taken at the center of the inclusion. Inclusion boundaries are clearly visible on this image.

Similar results were obtained for the second imaging plane displaced from the center but still within the inclusion. Fig. 7(b) corresponds to the last imaging plane 5 mm outside of the inclusion. Inclusion boundaries were not detected either in this or in the previous imaging plane outside of the inclusion.

Based on these images, the closed curve of constant Young's modulus is defined along the border of a 40 by 40 mm rectangle positioned at the center of this phantom, and elasticity reconstruction of the square area is performed at all four planes. The results are shown in Figs. 7(c)–(f) over exactly the same display dynamic range used in Fig. 6. In Fig. 7(c), the Young's modulus reconstruction in the central plane highlights the presence of the hard inclusion detected in Fig. 7(a). This is an expected result since a plane strain state is well approximated at this plane, and the image reasonably approximates that of the phantom with long hard inclusion. In the second closest plane [Fig. 7(d)] the inclusion is also detected by the reconstruction algorithm, although artifacts are slightly larger than on the previous image. Nevertheless, as soon as the imaging plane is outside of the inclusion,

the inclusion is not present on reconstructed images of the Young's modulus distribution [Figs. 7(e) and (f)]. Therefore, within 1-2 mm of the edge, images within and outside the inclusion [Figs. 7(d) and (e)] are recognizable although artifact levels are certainly higher. At only 5 mm beyond the edge of the inclusion, the reconstruction looks very much like the homogeneous phantom. Also, the level of artifacts is reduced for the last imaging plane [Fig. 7(f)] compared to the previous image [Fig. 7(e)] since the inclusion has less influence on displacement/strain fields. Note that the resolution in x_3 (i.e., slice thickness) of the strain imaging system is about 1.5-2 mm at the center of the inclusion. These results demonstrate that if uniform surface loading is used for phantom deformation, then reconstruction based on a model of a plane strain state [i.e., (13)] leads to reasonable results even if inhomogeneities are not infinite.

Finally, images of Γ and Π for the phantom with three hard inclusions of different sizes are presented in Fig. 8(a) and (b), respectively. In these images precisely the same parameters and display formats as in Fig. 4 and Fig. 5(a) and (b), respectively, were used. These images were computed for a step size $h = 0.4$ mm to highlight the fidelity of inclusion boundaries. All three inclusions are detected, where the distance between vertical boundaries closely approximates

(a)   (b)

(c)   (d)

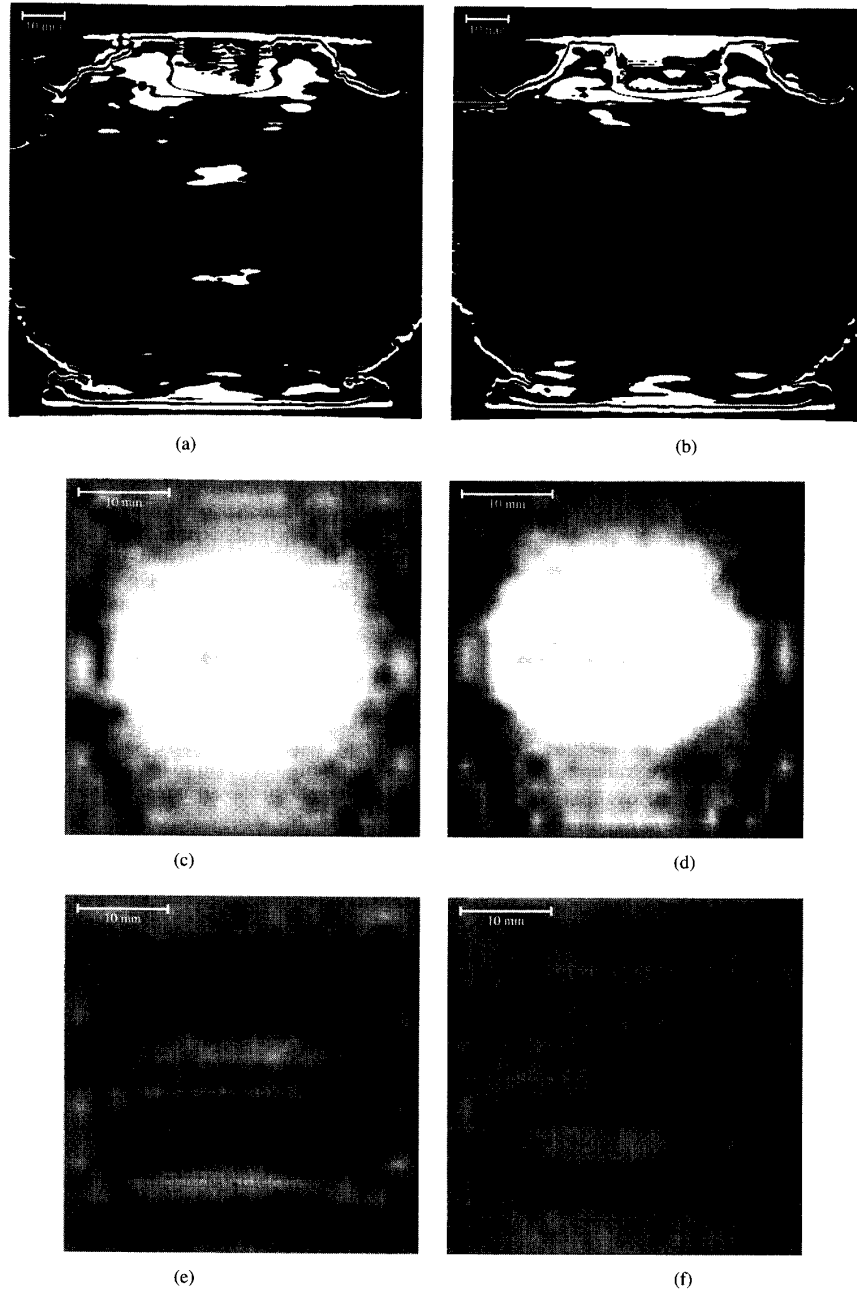(e)   (f)

Fig. 7.   Results of the hybrid Young's modulus reconstruction for the phantom with a short hard inclusion extending only 10 mm in length, i.e., less than 10% of the phantom length: (a) and (b) threshold differential elastic modulus (II) estimates for the imaging planes inside and outside of the inclusion, respectively, c–f) reconstructed Young's modulus distribution at four different planes within this phantom, as shown in Fig. 3C.

the actual physical dimensions of each inclusion. The reconstruction of the Young's modulus distribution of the smallest inclusion is presented in Fig. 8(c) for a 20 mm by 20 mm square with inclusion approximately in the center. The same logarithmic gray scale as in Fig. 6 ($0.5 < E/E_0 < 2.1$) is used. Again, the size of the detected inclusion closely corresponds to the actual size. However, even though the inclusion is noticeable in this image, the level of artifacts is comparable

with the magnitude of the inclusion's Young's modulus. Note that the spatial resolution of strain and displacement images is about half the diameter of this smallest inclusion.

V. DISCUSSION

Reconstructive elasticity imaging is possible if internal displacement and strain fields are accurately measured with
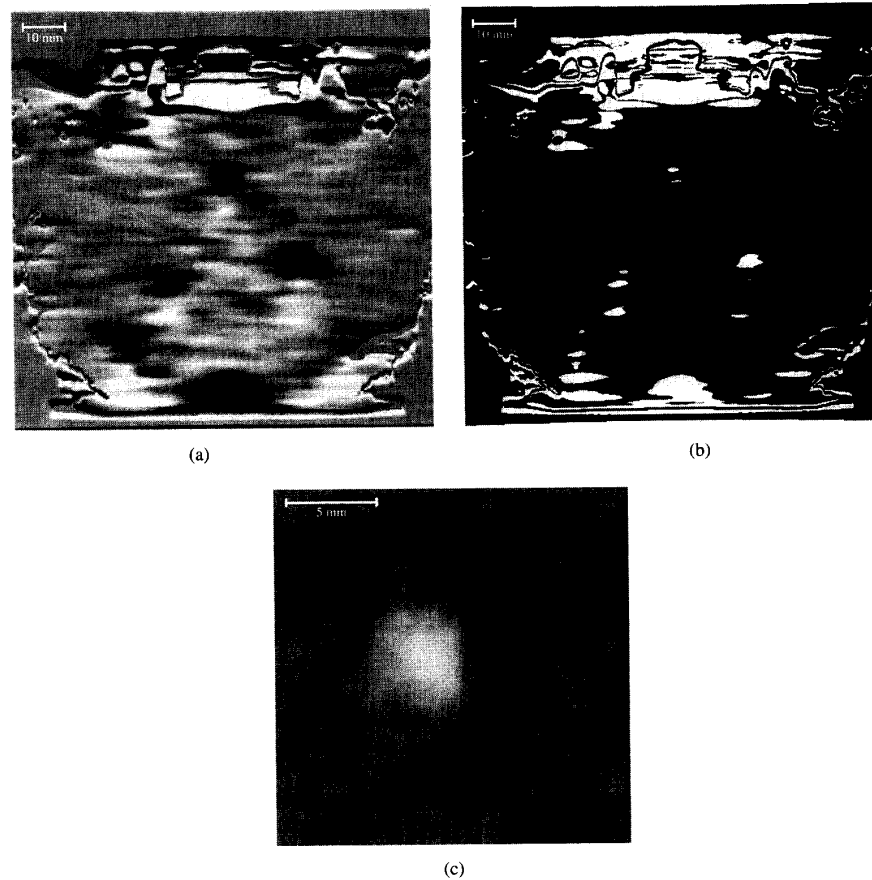
(a)

(b)

(c)

Fig. 8.   Results of the hybrid Young's modulus reconstruction for the phantom with three hard inclusions of different size: (a) normalized elastic modulus (Γ) estimate for a central cross sectional plane of the phantom, (b) threshold differential elastic modulus (Π) estimate, (c) reconstructed Young's modulus distribution for a 20 by 20 mm square positioned at the top of the phantom. This area includes a 6.5 mm diameter inhomogeneity located approximately in the center of the image.

subsequent reconstruction of the elastic (Young's) modulus. In this report, we have shown that longitudinal displacement and strain images in the limit of large (compared to an acoustic wavelength) surface deformation can be used to detect inclusion boundaries and reconstruct the Young's modulus distribution.

Boundaries of local inhomogeneities can be detected even in cases where the simple assumptions leading to (12) are not strictly valid. If a plane strain state can be approximated, then accurate estimates of Γ will be obtained from images of a single strain component at boundary points where the components of the normal vector are equal in magnitude, i.e., $(n_1)^2 = (n_2)^2$. Even at boundary points not satisfying this condition, either Γ or Π will still differ from unity although the exact value will be incorrect if the magnitude of the longitudinal strain is significant. At positions where either the magnitude of the shear strain is greater than that of the longitudinal strain or the longitudinal strain signal-to-noise (SNR) is poor, (12) cannot be used for boundary detection. Nevertheless, as demonstrated by measurements on simple gel-based phantoms, bounded inclusions can be readily detected with (12) if the longitudinal strain SNR is large.

The parameters Γ or Π are computed with a fixed step. For the results presented in Figs. 5(a) and (b), a step of 0.4 mm was used. This size is considerably less than the 3 mm spatial resolution of the original strain images [28], [29]. Such a small step size was used to minimize the apparent extent of inclusion boundaries. An unfortunate consequence is that both Γ and Π are severely underestimated. To gain more accurate measures of the relative Young's modulus at the boundary, a step size comparable to the spatial resolution must be chosen. In Fig. 5(d) the Π image for the phantom with a single soft inclusion is illustrated for a step size of 4 mm and a threshold such that $\Pi < 0.6$ is black and $\Pi \geq 0.6$ is white. Both top and bottom borders of the inclusion are highlighted, but without the fidelity of Fig. 5(b). Nevertheless, peak values of Π in the region where $(n_1)^2 = (n_2)^2$ are about 1.3, close to the value of $\Pi = 1.5$ (i.e., $\Gamma = 2.5$) expected for this inclusion. A comparison between Fig. 5(b) and (d) demonstrates the need to compute Π at several different step sizes. Small steps can delineate the boundaries of local abnormalities whereas large steps can quantify the Young's modulus along regions of the boundary where $(n_1)^2 \approx (n_2)^2$. If the inclusion itself is homogeneous, then elasticity reconstruction is complete

since Γ or Π is estimated in boundary areas where $(n_1)^2 \approx (n_2)^2$.

The Young's modulus at the inclusion boundary was calculated from a single accurately measured component of the strain tensor, where this estimate is only valid at points where $(n_1)^2 = (n_2)^2$. However, to fully characterize deformations of an elastic body, the complete displacement vector and strain tensor must be computed. For a plane strain state, only lateral and longitudinal components of the displacement vector must be measured since the other component vanishes. Consequently, only one longitudinal and one shear component of the strain tensor need be measured to represent the strain tensor for an incompressible material under a plane strain state. Parameters Γ or Π can be more accurately computed at **all** boundary points if every component of the strain (i.e., longitudinal and shear) is measured and the more general (11) is used.

If the inclusion is not homogeneous, boundary detection can aid more complete reconstruction. Once the boundary is determined and the modulus on that boundary estimated, more traditional numerical algorithms can be used to reconstruct the elasticity distribution within the inclusion. However, the specific approach used to solve second order partial differential equations of the type given in (13) depends on the relative magnitudes of the coefficients in the equation [40]. This equation generally is hyperbolic, although a degenerate (i.e., parabolic) case is possible. For an incompressible material, the degenerate case for the plane strain state corresponds to an in-plane translation with rotation of the volume as a rigid body. This means that the distribution of relative Young's modulus $k(\mathbf{X})$ cannot be reconstructed in this case without knowledge of the pressure distribution. Nevertheless, if the pressure distribution can be measured, then elasticity reconstruction can be performed directly.

Numerical solution of (13) for a nondegenerate case requires only knowledge of the elastic modulus along some boundary, but not necessarily the boundary of the object. Using inclusion boundaries determined by (12), the Young's modulus must be specified for any closed curve outside this inclusion. In general, however, Goursat conditions are preferable, where the Young's modulus need be specified only along two intersecting characteristic curves [40]. These characteristic curves reduce simply to two intersecting edges of a square region of interest if the ratio of shear strain to longitudinal is small over the ROI. Consequently, if the external deformation can be controlled to minimize the ratio of shear to longitudinal strain components in a square ROI, then the boundary conditions are greatly simplified. Future studies will explore Goursat conditions for geometries more closely approximating clinical imaging.

The quality of Young's modulus reconstruction is ultimately limited by the spatial resolution and accuracy of measured displacements and strains. Previously, a method of tracking relatively large displacements was presented showing significant signal-to-noise (SNR) improvement in both displacement and strain estimates [28]. These SNR improvements should enhance contrast resolution in elasticity reconstruction. That is, even if linear elasticity does not strictly hold for large scale deformations, Young's modulus reconstruction based on (12) and (13) may still be more accurate. To test this, the

entire set of experiments on the homogeneous phantom and phantoms with a single hard or soft inclusion was repeated with a uniform surface displacement of 13.2 mm, representing nearly a factor of 3 increase in the external deformation. Reconstructions based on these measurements are presented in Fig. 9 over the same display dynamic range used for Fig. 6. Again, Fig. 9(a) is the homogeneous phantom, Fig. 9(b) is the phantom with a single hard inclusion and Fig. 9(c) is the phantom with a single soft inclusion. A comparison of the results in Figs. 6 and 9 clearly demonstrates that contrast resolution in elasticity reconstructions is improved if larger external deformations are used. For more quantitative comparison, the profiles of the Young's modulus distribution along the central horizontal line of Figs. 6(a) and 9(a) (i.e., homogeneous phantom) are presented in Fig. 9(d). Significant reduction in Young's modulus variations due to enhanced SNR is noticeable in this graph. Therefore, SNR improvement in strain and displacement measurements directly translates into enhanced contrast resolution in elasticity reconstructions. To optimize both spatial and contrast resolution of elasticity images, deformational imaging methods permitting larger internal strains must be used for all applications.

In the present study, only one longitudinal component of the displacement vector was accurately measured in the imaging plane. However, the lateral u_1 displacement can be estimated directly from the measured longitudinal u_2 displacement using the principle of incompressibility, i.e., $u_{1,1} + u_{2,2} = 0$. With this condition, the lateral component was estimated assuming that it was zero along the central vertical line of the phantom. This is a good approximation for the experimental system and almost all phantoms used in the present study. In more general cases, however, this approximation may not hold and, therefore, accurate measurements of the lateral component of the displacement vector **at most** along any single vertical line are needed. In general, access to the lateral component of the displacement vector will significantly improve both reconstruction and boundary detection algorithms.

Even if strain images are intimately linked to the Young's modulus distribution, artifacts are present in these images due to the details of global boundary conditions, such as the geometry of the object, shape changes during deformation, specific types of external loads, etc. Reconstructive elasticity imaging has the potential to remove these artifacts and, therefore, produce images relatively independent of global boundary conditions. This is reasonable since no knowledge of the global boundary conditions is required to perform elasticity reconstruction in a selected ROI since linear elasticity specifies that true mechanical properties of a medium are not load/geometry dependent. At the same time, it has been demonstrated that the SNR in strain and displacement measurements has clear impact on elasticity images. Also, manipulations with global boundary conditions will permit proper control of the deformed state and, therefore, optimal balance between longitudinal and shear strain in the ROI. That is, careful control and optimization of the boundary conditions are necessary for accurate Young's modulus reconstruction even though reconstructions are theoretically independent of global boundary conditions.
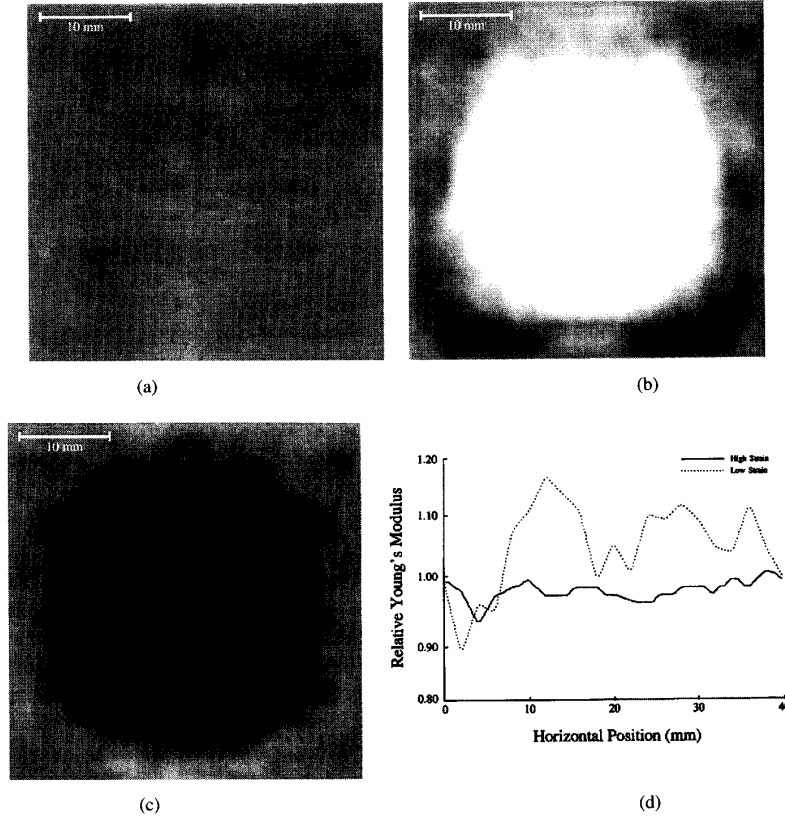
(a)

(b)

(c)

(d)

Fig. 9. Reconstructed images of the Young's modulus in the central plane of (a) homogeneous phantom, (b) phantom with a single hard inclusion, (c) phantom with a single soft inclusion. Phantoms were subjected to 13.2 mm uniform surface displacement, representing nearly a factor of 3 increase over the deformation used to produce Fig. 6. (d) Comparison of the reconstructed Young's modulus magnitude profiles in the homogeneous phantoms subjected to 4 and 13.2 mm surface displacements. These profiles along the central horizontal line of the corresponding image are plotted on a semi-logarithmic scale.

Finally, the results presented here suggest that quantitative reconstruction of the elastic modulus may be possible for complex objects such as the human body. Full reconstruction of the elastic properties of soft tissue without any assumptions should be based on reasonably good measurements of the complete 3-D spatial distribution of all necessary components of the displacement and strain. In the meantime, if limited measurements are available, then both a correct model of inhomogeneities and proper control of external deformation must be used for accurate reconstruction.

APPENDIX A
COMPRESSIBLE MEDIUM

In a compressible medium, the Poisson's ratio ν does not equal 0.5 and, therefore, the components of the stress tensor in an isotropic, continuous, compressible medium under static deformation are:

$$\sigma_{ij} = \lambda\Theta\delta_{ij} + 2\mu\varepsilon_{ij} \qquad \text{(A-1)}$$

where $\Theta = div\mathbf{U} = \varepsilon_{11} + \varepsilon_{22} + \varepsilon_{33}$ is the trace of the strain tensor, the parameters λ and μ are Lame coefficients, and ε_{ij} is one component of the strain tensor defined in (4). Note the differences between the stress-strain relations in (2) and (A-

1). Assuming that the Poisson's ratio depends only slightly on position, and defining the following parameters

$$l = \frac{\nu}{(1+\nu)(1-2\nu)}, \qquad m = \frac{1}{2(1+\nu)} \qquad \text{(A-2)}$$

the Lame coefficients can be written in the form

$$\lambda = lE_0 k(\mathbf{X}), \qquad \mu = mE_0 k(\mathbf{X})$$

where E_0 is constant and $k(\mathbf{X})$ is arbitrary and not generally a continuous function of position.

First we will consider a bounded inclusion with boundary $\mathbf{G}$. Assigning indexes "int" and "ext" to internal and external variables, respectively, at boundary points, and substituting Γ for the ratio of Young's moduli E^{ext}/E^{int}, the stress continuity condition (7) becomes [26]:

$$\Gamma[l\Theta^{ext}n_1 + 2m(\varepsilon_{11}^{ext}n_1 + \varepsilon_{12}^{ext}n_2 + \varepsilon_{13}^{ext}n_3)]$$
$$= l\Theta^{int}n_1 + 2m(\varepsilon_{11}^{int}n_1 + \varepsilon_{12}^{int}n_2 + \varepsilon_{13}^{int}n_3)$$
$$\Gamma[l\Theta^{ext}n_2 + 2m(\varepsilon_{12}^{ext}n_1 + \varepsilon_{22}^{ext}n_2 + \varepsilon_{23}^{ext}n_3)]$$
$$= l\Theta^{int}n_2 + 2m(\varepsilon_{12}^{int}n_1 + \varepsilon_{22}^{int}n_2 + \varepsilon_{23}^{int}n_3)$$
$$\Gamma[l\Theta^{ext}n_3 + 2m(\varepsilon_{13}^{ext}n_1 + \varepsilon_{23}^{ext}n_2 + \varepsilon_{33}^{ext}n_3)]$$
$$= l\Theta^{int}n_3 + 2m(\varepsilon_{13}^{int}n_1 + \varepsilon_{23}^{int}n_2 + \varepsilon_{33}^{int}n_3). \qquad \text{(A-3)}$$

Note the similarity of (A-3) with (8) for an incompressible material. Again, if all components of the strain tensor are known, then any equation in (A-3) can be used to determine Γ at the inclusion boundary, and the other two equations in (A-3) can be used to estimate the accuracy of strain measurements in the neighborhood of the boundary point. However, if the value of Poisson's ratio is unknown, i.e., parameters l and m cannot be computed and must be eliminated from the system of equations (A-3), the resulting equations will be the same as in (9). This is an expected result since in both compressible and incompressible media the same $\lambda\Theta$ product must be eliminated. Nevertheless, if the elastic properties do not exhibit large fluctuations inside the inclusion, elasticity reconstruction is complete since the value of $k(\mathbf{X})$ is found at the inclusion boundary.

If the function $k(\mathbf{X})$ is continuous with well defined spatial derivatives, then complete reconstruction of the elasticity within the region of interest must be performed. For this case, the equilibrium condition (1) can be rewritten in the form [26]

$$E_0 k(l\Theta_{,1} + 2m\varepsilon_{11,1} + 2m\varepsilon_{12,2} + 2m\varepsilon_{13,3})$$
$$+ E_0(l\Theta k_{,1} + 2m\varepsilon_{11}k_{,1} + 2m\varepsilon_{12}k_{,2} + 2m\varepsilon_{13}k_{,3}) + f_1 = 0$$
$$E_0 k(l\Theta_{,2} + 2m\varepsilon_{12,1} + 2m\varepsilon_{22,2} + 2m\varepsilon_{23,3})$$
$$+ E_0(l\Theta k_{,2} + 2m\varepsilon_{12}k_{,1} + 2m\varepsilon_{22}k_{,2} + 2m\varepsilon_{23}k_{,3}) + f_2 = 0)$$
$$E_0 k(l\Theta_{,3} + 2m\varepsilon_{13,1} + 2m\varepsilon_{23,2} + 2m\varepsilon_{33,3})$$
$$+ E_0(l\Theta k_{,3} + 2m\varepsilon_{13}k_{,1} + 2m\varepsilon_{23}k_{,2} + 2m\varepsilon_{33}k_{,3})$$
$$+ f_3 = 0. \tag{A-4}$$

Here the lower index after a comma means differentiation with respect to the corresponding spatial coordinate.

It is important to note that each equation in (A-4) is only a first order partial differential equation with respect to $k(\mathbf{X})$ and, therefore, generally more preferable. However, the specific equations presented here for a compressible medium are very difficult to solve if in fact the medium is nearly incompressible. In this case, $\Theta = div\,\mathbf{U}$ is small, but the parameter l is large (since Poisson's ratio ν is very close to 0.5 for a slightly compressible medium). Consequently, the effect of very small errors in estimating Θ from deformation measurements can be greatly magnified by multiplication with l.

Similar to an incompressible material, parameter $l\Theta$ can be eliminated from (A-4), and the system of equations (10) will be obtained with the following changes in notation:

$$F_{12} = (f_{2,1} - f_{1,2})/mE_0,$$
$$F_{13} = (f_{3,1} - f_{1,3})/mE_0,$$
$$F_{23} = (f_{3,2} - f_{2,3})/mE_0.$$

Each equation in (10), however, is a second order partial differential equation with respect to $k(\mathbf{X})$, and requires knowledge of higher strain and displacement derivatives than in (A-4). Since these components are measured with finite signal-to-noise ratio, error due to higher derivatives may increase.

If all components of the displacement and strain are available, hybrid reconstruction of the Young's modulus proceeds

as outlined before. First, strain and displacement images are processed to highlight boundaries between regions of different elastic modulus. This is based on either (A-3) or (9). If the inclusion is clearly bounded, then elasticity reconstruction is complete. Spatial variations of the elasticity inside the region of interest (ROI) are computed following boundary detection. After low pass filtering both displacement and strain data within the ROI to ensure a continuous elasticity distribution, the reconstruction is performed by numerically solving either (A-4) or (10). This will conclude elasticity reconstruction within that ROI.

Again, a specific type of applied deformation can be considered requiring displacement and strain data only in the imaging $(x_1, x_2, 0)$ plane. For a plane strain state, the last equation in (A-3) is satisfied since $n_3 = 0$ for this case, and the first two equations in (A-3) reduce to

$$\Gamma = \frac{l\Theta^{int}n_1 + 2m(\varepsilon_{11}^{int}n_1 + \varepsilon_{12}^{int}n_2)}{l\Theta^{ext}n_1 + 2m(\varepsilon_{11}^{ext}n_1 + \varepsilon_{12}^{ext}n_2)}$$
$$\Gamma = \frac{l\Theta^{int}n_2 + 2m(\varepsilon_{12}^{int}n_1 + \varepsilon_{22}^{int}n_2)}{l\Theta^{ext}n_2 + 2m(\varepsilon_{12}^{ext}n_1 + \varepsilon_{12}^{ext}n_2)}. \tag{A-5}$$

Also, if the parameter $l\Theta$ must be eliminated from (A-5), then (11) will be obtained. Both (A-5) and (11) should be satisfied along the boundary of a clearly bounded inclusion. Note that these equations can also be used for boundary detection.

For a plane strain state, (A-4) reduces to two nontrivial equations:

$$E_0 k(l\Theta_{,1} + 2m\varepsilon_{11,1} + 2m\varepsilon_{12,2})$$
$$+ E_0(l\Theta k_{,1} + 2m\varepsilon_{11}k_{,1} + 2m\varepsilon_{12}k_{,2}) + f_1 = 0$$
$$E_0 k(l\Theta_{,2} + 2m\varepsilon_{12,1} + 2m\varepsilon_{22,2})$$
$$+ E_0(l\Theta k_{,2} + 2m\varepsilon_{12}k_{,1} + 2m\varepsilon_{22}k_{,2}) + f_2 = 0)$$
$$f_3 = 0. \tag{A-6}$$

For the case of a slightly compressible media, (10), with notations for compressible media, reduces to one nontrivial equation similar to (13). Again, two-dimensional in-plane displacement/strain measurements are needed to reconstruct the Young's modulus in the plane $x_3 = 0$ if either (A-6) or (13) is used.

In conclusion, incompressible and slightly compressible media must be treated in a similar way, since strain and displacement components are measured with finite accuracy and, consequently, small error in these measurements may have large impact on the elasticity reconstruction. However, if the media is compressible, then equations with lower order derivatives can be used.

APPENDIX B
SIMPLIFICATIONS FROM SPATIAL SYMMETRIES

Along with simplifications of a general model for elasticity reconstruction due to careful control of the deformed state, other simplifications from spatial symmetries are possible. Below, we present several types of 3-D inclusions possessing

simple symmetries where the problem reduces to a condition similar to (11) in the particular plane. For these symmetric inclusions, however, many points satisfy the condition $n_3 = 0$, similar to a plane strain state. In all cases considered here, it was assumed that strain and displacement data are measured in the imaging plane $(x_1, x_2, 0)$, i.e. $x_3 = 0$.

If the inclusion has a plane of symmetry, i.e., there is a plane $(x_1, x_2, 0)$ crossing the inclusion such that along the boundary the condition $n_3 = 0$ is fulfilled, then at every point on that boundary, with no assumption about the deformed state of the volume V, the first equation of (9) leads to (11), repeated here for convenience:

$$\Gamma = \frac{n_1 n_2 (\varepsilon_{11}^{int} - \varepsilon_{22}^{int}) + [(n_2)^2 - (n_1)^2] \varepsilon_{12}^{int}}{n_1 n_2 (\varepsilon_{11}^{ext} - \varepsilon_{22}^{ext}) + [(n_2)^2 - (n_1)^2] \varepsilon_{12}^{ext}}.$$

In this equation, n_1 and n_2 are two orthogonal components of the normal vector $\mathbf{n} = (n_1, n_2, 0)$ to the inclusion boundary in plane (x_1, x_2), and all terms in this equation can be directly obtained from 2-D measurements in the imaging plane. If the inclusion changes shape slightly along the x_3 direction making the n_3 component nonzero but small in some regions of the imaging plane, then terms in the first equation of (9) containing n_3 are also small such that (11) still accurately models the stress continuity requirements for these regions. This is, for example, why boundary detection based on (12) for the phantom with a short hard inclusion highlights the borders of such an inclusion even if the plane strain state approximation is weak. The ultimate accuracy depends on the relative magnitude of the out-of-plane shear strain ε_{13} and ε_{23} with respect to in-plane ε_{11}, ε_{22}, and ε_{12} strain components.

For an inclusion with planar symmetry, the spatial distribution of Young's modulus should satisfy the condition $k(x_1, x_2, x_3) = k(x_1, x_2, -x_3)]$. Then, the first equation of (10) for the plane $(x_1, x_2, 0)$ takes the form:

$$2\varepsilon_{12}(k_{,11} - k_{,22}) + 2(u_{2,2} - u_{1,1})k_{,12}$$
$$+ (\Delta_3 u_2 + u_{2,33} + \omega_{12,1})k_{,1} - (\Delta_3 u_1 + u_{1,33}$$
$$- \omega_{12,2})k_{,2}$$
$$+ \Delta_3 \omega_{12} k + \omega_{12,33} k + F_{12} = 0 \qquad \text{(B-1)}$$

where

$$\omega_{12} = u_{2,1} - u_{1,2},$$
$$\Delta_3 = \partial^2/(\partial x_1^2) + \partial^2/(\partial x_2^2),$$
$$F_{12} = (3/E_0)(f_{2,1} - f_{1,2}).$$

The out-of-plane displacement component u_3 has been eliminated in this equation, and other components of the displacement/strain can be computed from 2-D measurements in the imaging plane. However, terms $u_{1,33}$, $u_{2,33}$ and $\omega_{12,33}$ cannot be computed from measurements in a single imaging plane only, and create reconstruction error if ignored. Nevertheless, if measurements are possible in three close parallel imaging planes, then second order derivatives can be found for a central imaging plane using a finite difference approximation and, consequently, included in the reconstruction algorithm.

In general, however, the magnitude of these terms can be minimized by carefully controlling the deformed state of the medium. In particular, the plane strain state is one such controlled deformation.

If the inclusion has axial symmetry, for example an x_1-axis symmetrical inhomogeneity, where relative Young's modulus $k(\mathbf{X})$ and inclusion boundary $\mathbf{G}$ take the forms

$$k(x_1, x_2, x_3) = k(x_1, r),$$
$$\mathbf{G} : g(x_1, r) = 0,$$
$$r^2 = (x_2)^2 + (x_3)^2,$$

then the first equation of (9) for the imaging plane $x_3 = 0$ will lead to

$$\Gamma = \frac{rx_2 g_{,1} g_{,r} (\varepsilon_{11}^{int} - \varepsilon_{22}^{int}) + [(x_2 g_{,r})^2 - (rg_{,1})^2] \varepsilon_{12}^{int}}{rx_2 g_{,1} g_{,r} (\varepsilon_{11}^{ext} - \varepsilon_{22}^{ext}) + [(x_2 g_{,r})^2 - (rg_{,1})^2] \varepsilon_{12}^{ext}}.$$

Again, all terms in this equation can be directly computed from measured strain components in the imaging plane. Note that no assumption is made about the deformed state.

For actual reconstruction of the Young's modulus $k(\mathbf{X})$, the first equation of (10) in the imaging plane $x_3 = 0$ and, therefore, $r = x_2$, leads to an expression identical to (B-1) permitting measurements in three close parallel planes to access out-of-plane derivatives. Similar results can be obtained for an inclusion with x_2-axis of symmetry, i.e.,

$$k(x_1, x_2, x_3) = k(x_2, r),$$
$$\mathbf{G} : g(x_2, r) = 0,$$
$$r^2 = (x_1)^2 + (x_3)^2.$$

Finally, a spherically symmetric inhomogeneity is a particular case of the axially symmetric inclusion considered above with spatial distribution of Young's modulus

$$k(x_1, x_2, x_3) = k(r), \quad r^2 = (x_1)^2 + (x_2)^2 + (x_3)^2.$$

Here, for an arbitrary deformed state of volume V, the first equation of (9) for the plane $x_3 = 0$ reduces to a second order linear ordinary differential equation rather than a second order partial differential equation (B-1)

$$\frac{2}{r^2} \left(k_{,rr} - \frac{1}{r} k_{,r} \right) [(x_1^2 - x_2^2)\varepsilon_{12} + x_1 x_2 (u_{2,2} - u_{1,1})]$$
$$+ \frac{1}{r} k_{,r} [x_1 (\Delta_3 u_2 + u_{2,33} + \omega_{12,1})$$
$$- x_2 (\Delta_3 u_1 + u_{1,33} - \omega_{12,2})]$$
$$+ k(\Delta_3 \omega_{12} + \omega_{12,33}) + F_{12} = 0 \qquad \text{(B-2)}$$

which has a simple form for $x_1 = r$, $x_2 = 0$:

$$2\varepsilon_{12} \left(k_{,rr} - \frac{1}{r} k_{,r} \right) + k_{,r} (\Delta_3 u_2 + u_{2,33} + \omega_{12,1})$$
$$+ k(\Delta_3 \omega_{12} + \omega_{12,33}) + F_{12} = 0.$$

Again, all terms containing second order partial derivatives with respect to x_3 can either be obtained from measurements of

corresponding displacement/strain components in three close parallel planes, or ignored if the deformed state is controlled so that these terms vanish.

In practice, however, neither a perfect plane strain state nor symmetric inhomogeneities may exist. Full reconstruction of the elastic properties of soft tissue without any assumptions should be based on complete 3-D measurements of all necessary displacement and strain components. If only limited measurements are available, then both a correct model of inhomogeneities and careful control of external deformations must be used to achieve a reasonably accurate reconstruction.

ACKNOWLEDGMENT

REFERENCES

[1] R. J. Dickinson and C. R. Hill, "Measurement of soft tissue motion using correlation between A-scans," Ultrasound Med. Biol., vol. 8, pp. 263–271, 1982.
[2] A. Eisensher, E. Schweg-Toffler, G. Pelletier, and G. Jacquemard, "La palpation echographique rythmee—Echosismographie," J. Radiologie, vol. 64, pp. 225–261, 1983.
[3] M. Tristam, D. C. Barbosa, D. O. Cosgrove, D. K. Nassiri, J. C. Bamber, and C. R. Hill, "Ultrasonic study of in vivo kinetic characteristics of human tissue," Ultrasound Med. Biol., vol. E12, pp. 927–937, 1986.
[4] T. A. Krouskop, D. R. Dougherty, and S. F. Levinson, "A pulsed Doppler ultrasonic system for making noninvasive measurements of the mechanical properties of soft tissue," J. Rehabil. Res. Dev., vol. 24, no. 2, pp. 1–8, 1987.
[5] M. Tristam, D. C. Barbosa, D. O. Cosgrove, J. C. Bamber, and C. R. Hill, "Application of Fourier analysis to clinical study of patterns of tissue movement," Ultrasound Med. Biol., vol. 14, no. 8, pp. 695–707, 1988.
[6] J. Meunier and M. Bertrand, "Ultrasonic speckle motion inherent to tissue motion: Theory and simulation," in Proc. 1989 IEEE Ultrason. Symp., 1989, vol. 0090-5607-89, pp. 865–868.
[7] L. Axel and L. Dougherty, "Heart wall motion: Improved method of spatial modulation of magnetization for MR imaging," Radiology, vol. 169, pp. 59–63, 1988.
[8] E. A. Zerhouni, D. M. Parish, W. J. Rogers, A. Yang, and E. P. Shapiro, "Human heart: Tagging with MR imaging—A method for noninvasive assessment of myocardial motion," Radiology, vol. 169, pp. 164–172, 1988.
[9] R. S. Adler, J. M. Rubin, P. H. Bland, and P. L. Carson, "Characterization of transmitted motion in fetal lung: Quantitative analysis," Med. Phys., vol. 16, no. 3, pp. 333–337, 1989.
[10] M. Bertrand, J. Meunier, M. Doucet, and G. Ferland, "Ultrasonic biomechanical strain gauge based on speckle tracking," in Proc. 1989 IEEE Ultrason. Symp., 1989, vol. 0090-5607-89, pp. 859–864.
[11] R. S. Adler, J. M. Rubin, P. H. Bland, and P. L. Carson, "Quantitative tissue motion analysis of digitized M-mode images: Gestational differences of fetal lung," Ultrasound Med. Biol., vol. 16, no. 6, pp. 561–569, 1990.
[12] R. M. Lerner, S. R. Huang, and K. J. Parker, "Sonoelasticity" images derived from ultrasound signals in mechanically vibrated tissues," Ultrasound Med. Biol., vol. 16, no. 3, pp. 231–239, 1990.
[13] K. J. Parker, S. R. Huang, R. A. Musulin, and R. M. Lerner, "Tissue response to mechanical vibrations for "sonoelasticity imaging"," Ultrasound Med. Biol., vol. 16, no. 3, pp. 241–246, 1990.
[14] Y. Yamakoshi, J. Sato, and T. Sato, "Ultrasonic imaging of the internal vibration of soft tissue under forced vibration," IEEE Trans. Ultrason. Ferroelect. and Freq. Cont., vol. 37, pp. 45–53, 1990.
[15] Y. Yamashita and M. Kubota, "Tissue characterization from ultrasonic imaging of movement and deformation," in Procs. 1990 Ultrasonics Symp., 1990, vol. 2, pp. 1371–1375.

[16] A. P. Sarvazyan and A. R. Skovoroda, "The new approaches in ultrasonic visualization of cancers and their qualitative mechanical characterization for the differential diagnostics," in Abstract of the All-Union Conference The Actual Problems of the Cancer Ultrasonic Diagnostics, 1990.
[17] J. Ophir, I. Cespedes, H. Ponnekanti, Y. Yazdi, and X. Li, "Elastography: A quantitative method for imaging the elasticity of biological tissues," Ultrasonic Imag., vol. 13, pp. 111–134, 1991.
[18] M. O'Donnell, A. R. Skovoroda, and B. M. Shapo, "Measurement of arterial wall motion using Fourier based speckle tracking algorithms," in Proc. 1991 IEEE Ultrason. Symp., 1991, vol. 91CH3079, pp. 1101–1104.
[19] F. Lee, J. P. Bronson, R. M. Lerner, K. J. Parker, S. R. Huang, and D. J. Roach, "Sonoelasticity imaging: Results in in vitro tissue specimens," Radiology, vol. 181, pp. 237–239, 1991.
[20] A. P. Sarvazyan and A. R. Skovoroda, "Tissue characterization in medical imaging in terms of viscoelastic mechanical properties," in abstract of 6th World Congr. in Ultrasound, 1991.
[21] H. Ponnekanti, J. Ophir, and I. Cespedes, "Axial stress distributions compressors in elastography: An analytical model," Ultrasound Med. Biol., vol. 18, no. 8, pp. 667–673, 1992.
[22] L. K. Ryan, G. R. Lockwood, B. G. Starkoski, D. W. Holdsworth, D. W. Rickey, M. Drangova, A. Fenster, and F. S. Foster, "A high frequency intravascular imaging system for investigation of vessel wall properties," in Proc. 1992 IEEE Ultrasonics Symp., 1992, vol. 1051-0117-92, pp. 1101–1105.
[23] S. Y. Yemelyanov, A. R. Skovoroda, M. A. Lubinski, B. M. Shapo, and M. O'Donnell, "Ultrasound elasticity imaging using Fourier based speckle tracking algorithm," in Proc. 1992 IEEE Ultrason. Symp., 1992, vol. 2, pp. 1065–1068.
[24] J. B. Fowlkes, S. Y. Yemelyanov, J. G. Pipe, P. L. Carson, R. S. Adler, A. P. Sarvazyan, and A. R. Skovoroda, "Possibility of cancer detection by means of measurement of elastic properties," Radiology, vol. 185, no. P, pp. 206–207, 1992.
[25] E. J. Chen, W. K. Jenkins, and W. D. O'Brien, "The accuracy and precision of estimating tissue displacement from ultrasonic images," in Proc. 1992 IEEE Ultrason. Symp., 1992, vol. 2, pp. 1061–1064.
[26] A. R. Skovoroda, Inverse Problems of the Theory of Elasticity in the Diagnostics of Soft Tissue Pathologies, Pushchino: Pushchino Research Center of Russian Academy of Sciences, 1992.
[27] M. O'Donnell, S. Y. Emelianov, A. R. Skovoroda, M. A. Lubinski, W. F. Weitzel, and R. C. Wiggins, "Quantitative elasticity imaging," in Proc. 1993 IEEE Ultrason. Symp., 1993, vol. 93CH3301-9, pp. 893–903.
[28] M. O'Donnell, A. R. Skovoroda, B. M. Shapo, and S. Y. Emelianov, "Internal displacement and strain imaging using ultrasonic speckle tracking," IEEE Trans. Ultrason. Ferroelect. and Freq. Cont., vol. 41, pp. 314–325, 1994.
[29] A. R. Skovoroda, S. Y. Emelianov, M. A. Lubinski, A. P. Sarvazyan, and M. O'Donnell, "Theoretical analysis and verification of ultrasound displacement and strain imaging," IEEE Trans. Ultrason. Ferroelect. and Freq. Cont., vol. 41, pp. 302–313, 1994.
[30] S. Y. Emelianov, A. R. Skovoroda, M. A. Lubinski, and M. O'Donnell, "Reconstructive elasticity imaging," to appear in J. P. Jones, Ed. Acoustical Imaging. New York: Plenum Press, 1994, vol. 21.
[31] A. P. Sarvazyan, A. R. Skovoroda, S. Y. Emelianov, J. B. Fowlkes, J. G. Pipe, R. S. Adler, R. B. Buxton, and P. L. Carson, "Biophysical bases of elasticity imaging," to appear in J. P. Jones, Ed. Acoustical Imaging. New York: Plenum Press, 1994, vol. 21.
[32] S. Y. Emelianov, M. A. Lubinski, W. F. Weitzel, R. C. Wiggins, A. R. Skovoroda, and M. O'Donnell, "Elasticity imaging for early detection of renal pathologies," accepted for publication in Ultrasound in Medicine and Biology, 1994.
[33] L. D. Landau and E. M. Liftshitz, Theory of Elasticity. Moscow: Nauka, 1965.
[34] Y. N. Rabotnov, Mechanics of Solid Structures.Moscow: Nauka, 1979.
[35] Y. C. Fung, Biomechanics-Mechanical Properties of Living Tissues. New York: Springer-Verlag, 1981.
[36] A. P. Sarvazyan, "Low frequency acoustical characteristics of biological tissues," Mechanics of Polymers, vol. 4, pp. 691–695, 1975.
[37] M. A. Biot, Mechanics of Incremental Deformations.New York: Wiley, 1965.
[38] F. A. Duck, Physical Properties of Tissues.San Diego, CA: Academic Press, 1990.
[39] A. E. Green and J. E. Adkins, Large Elastic Deformations and Nonlinear Continuum Mechanics. Oxford, UK: Clarendon Press, 1960.
[40] G. A. Korn and M. S. Korn, Mathematical Handbook for Scientists and Engineers. New York: McGraw-Hill, 1968.

A. R. Skovoroda received the B.S. and M.S. degrees in mathematics and mechanics in 1973 and 1975, respectively, from the Novosibirsk State University (USSR), and the Ph.D. degree in 1985 from the Moscow State University (USSR).

From 1975 to 1977 he was a lecturer in Theoretical Mechanics at the College of Textile Technology (Barnaul, USSR). From 1977 to 1980 he was a Ph.D. Researcher at the subfaculty of Plasticity of the Moscow State University, where he worked on the dynamic behavior of plates under blast-type loading. In 1981 he held an appointment as a Junior Research Associate at the Laboratory of Mathematical Modeling of the Research Computing Center of the USSR Academy of Sciences (the present name is the Institute of Mathematical Problems of Biology, Russian Academy of Sciences), where he developed efficient mathematical methods to solve the differential equations of the theory of elasticity. In 1986 he became a Senior Research Associate and was Scientific Secretary at the same Institute from 1988 to 1993. He is currently Head of the Laboratory of Mathematical Problems in Biomechanics and works on the biomechanics of soft tissue. Dr. A. Skovoroda has authored and co-authored more than 50 articles for archival publications and papers that were presented at All-Union and International meetings.

S. Y. Emelianov received the B.S. and M.S. degrees in physics in 1986 and 1989, respectively, from the Moscow State University, and the Ph.D. degree in physics in 1993 from Moscow State University, and the Institute of Mathematical Problems of Biology of the Russian Academy of Sciences, Russia.

In 1989, he joined the Institute of Mathematical Problems of Biology, where he was engaged in both mathematical modeling of soft tissue biomechanics and experimental studies of noninvasive methods in medical diagnostics based on tissue elasticity variations. Following his graduate work, he moved to University of Michigan, Ann Arbor, as a Post-Doctoral Fellow in the Electrical Engineering and Computer Science Department working on applications of imaging systems for medical diagnosis and nondestructive testing. Dr. Emelianov is currently a Research Associate at the Biomedical Ultrasonics Laboratory at the University of Michigan and involved primarily in the theoretical and practical aspects of ultrasound elasticity imaging. He is author of several scientific papers. His research interests are in the areas of tissue biomechanics, medical imaging systems and nondestructive material testing.

M. O'Donnell (M'70–SM'84–F'93), for biography, see p. 82 of the January issue of this TRANSACTIONS.